MATERIALS SCIENCE

All-in-one flexible supercapacitor with ultrastable performance under extreme load

You Wan Na[1]†, Jae Yeong Cheon[2]†, Jae Ho Kim[1]†, Yeonsu Jung[2], Kyunbae Lee[2], Jae Seo Park[1], Ji Yong Park[1], Ki Su Song[1], Sang Bok Lee[2], Taehoon Kim[2]*, Seung Jae Yang[1]*

Fiber-type solid-state supercapacitors are being widely investigated as stable power supply for next-generation wearable and flexible electronics. Integrating both high charge storage capability and superior mechanical properties into one fiber is crucial to realize fiber-type solid-state supercapacitors. In this study, we design a "jeweled necklace"–like hybrid composite fiber comprising double-walled carbon nanotube yarn and metal-organic frameworks (MOFs). Subsequent heat treatment transforms MOFs into MOF-derived carbon (MDC), thereby maximizing energy storage capability while retaining the superior mechanical properties. The hybrid fibers with tunable properties, including thickness and MDC loading amount, exhibit a high energy density of 7.54 milliwatt-hour per cubic centimeter at a power density of 190.94 milliwatt per cubic centimeter. The mechanical robustness of the hybrid fibers allows them to operate under various mechanical deformation conditions. Furthermore, it is demonstrated that the resulting superstrong fiber delivers sufficient power to switch on light-emitting diodes by itself while suspending 10-kilogram weight.

INTRODUCTION

Rapidly increasing demands for next-generation portable and flexible electronics, including roll-up displays and wearable devices, have stimulated intensive efforts to produce flexible, lightweight, and robust energy storage devices that can sustain high power and energy densities (*1*–*3*). Fiber-type solid-state supercapacitors are widely used to realize next-generation energy storage devices because of their flexibility, light weight, and ease of handling and metamorphosis (*4*–*6*). Various strategies have been explored, such as enlarging charge storage sites by supplementing porous materials, facilitating charge transport by using highly conductive materials along with pathway construction, and strengthening of fibers through reinforcement with robust materials for a viable fiber-type platform (*7*–*11*). However, these strategies have yielded only modest performance improvements because of being forced to consolidate unnecessary additives. Therefore, developing an integrated fiber that can store a large amount of charge, while exhibiting high conductivity and superior mechanical properties, is the crucial next step to develop next-generation electronics (*12*, *13*).

Here, we develop an "all-in-one" fiber with excellent electrical conductivity and superior mechanical properties that maintains a high specific surface area (SSA) and provides charge storage sites by fabricating a heterogeneous hybrid composite between carbon nanotube yarn (CNTY) and metal-organic frameworks (MOFs). Hydrothermal reaction enables the growth of bulky MOFs on the surface of double-walled CNTY (DWNTY), and subsequent heat treatment pyrolyzes the MOFs into MOF-derived carbons (MDCs) without compromising electrical and mechanical properties of DWNTY. The hybrid fiber with a controllable thickness and MDC loading density can stably deliver a high energy density of 7.54 mWh cm^{-3} at a power density of 190.94 mW cm^{-3} without metal electrodes while featuring high deformability. Notably, the fiber delivers sufficient power to switch on a light-emitting diode (LED) bulb even under a weight loading of 10 kg, which is the severest reported testing condition among fiber-type supercapacitors.

RESULTS

Background on a new class of hybrid composite between CNTYs and MDCs

The main idea for the structural design is to use an extremely strong and conductive DWNTY as the basic component and then decorate its outer surface with microporous MDCs to fabricate a fiber-type supercapacitor, thereby integrating both the structural and energy storage parameters into one fiber. Some groups have attempted to incorporate additives into the internal structure of the nanocarbon assemblies to enhance energy storage; however, this approach could be detrimental to the superb mechanical and transport properties of the nanocarbon assemblies.

Hybrid composites were fabricated by directly spinning the DWNTs and combining them into a single fiber, with thickness in the range of tens of micrometers, as schematically illustrated in Fig. 1A. Isoreticular MOF-1 (IRMOF-1) was initially investigated as a surface decorator of the DWNTYs because of its previously reported growth through heteronucleation predominantly occurring on the CNT surface through a hydrothermal reaction (*14*–*16*). Subsequently, the hybrid structure carbonized to transform the insulating IRMOF-1 into conductive microporous carbons (MDC-1) (*17*). Hybrid composite fibers were denoted as M1(concentration of precursor)@DW(ply) and C1(concentration of precursor)@DW(ply) for IRMOF-1 and MDC-1, respectively. This structural design facilitates direct external exposure of the highly porous carbons, thereby functioning as a high-energy and power storage system, without hampering the superior mechanical and electrical conductivity of DWNTY.

[1]Advanced Nanohybrids Laboratory, Department of Chemistry and Chemical Engineering, Education and Research Center for Smart Energy and Materials, Inha University, Incheon 22212, Republic of Korea. [2]Composites Research Division, Korea Institute of Materials Science (KIMS), Changwon 51508, Republic of Korea.
*Corresponding author. Email: sjyang@inha.ac.kr (S.J.Y.); tkim67@kims.re.kr (T.K.)
†These authors contributed equally to this work.

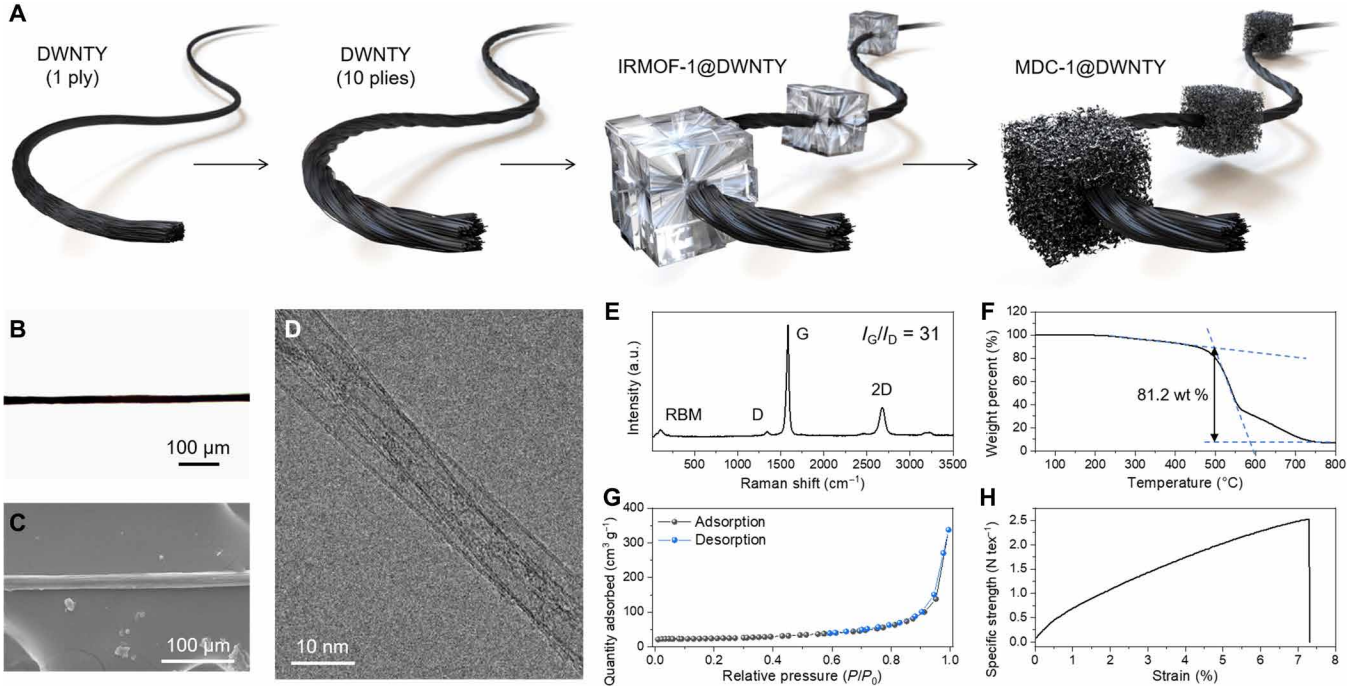

Fig. 1. Basic properties of DWNTY. (**A**) Schematics illustrating the fabrication method to prepare MDC-1@DWNTY, (**B**) optical microscopy (OM) image, (**C**) scanning electron microscopy (SEM) image, (**D**) transmission electron microscopy (TEM) image, (**E**) Raman spectrum, radial breathing mode (RBM), (**F**) thermogravimetric analysis (TGA), (**G**) N_2 sorption isotherm, and (**H**) stress-strain curve of DWNTY. a.u., arbitrary units; wt %, weight %.

Decorating the external surface of DWNTY with microporous carbons through heteronucleation of MOFs

After a floating catalyst-based synthesis, DWNTY was continuously produced by direct spinning and subsequently used to fabricate hybrid composite (fig. S1). As-produced DWNTY was immersed in acetone to densify and strengthen DWNTY. A DWNTY with a diameter of 15 μm comprises thousands of individual DWNTs with diameters of 5 nm, as shown in optical microscopy (OM), scanning electron microscopy (SEM), and transmission electron microscopy (TEM) images (Fig. 1, B to D, and fig. S2). Raman spectroscopy and thermogravimetric analysis (TGA) were used to confirm the high crystallinity and purity of the produced DWNTYs (Fig. 1, E and F) (*18*). The textural properties were analyzed by cryogenic N_2 sorption, revealing a type II isotherm of the highly integrated DWNTY (Fig. 1G) (*19*). The density of DWNTY after acetone densification was 1.175 g cm^{-3} with a high specific strength of 2.53 N tex^{-1} (Fig. 1H). Notably, DWNTY exhibited an excellent electrical conductivity of 14,310 S cm^2 g^{-1}, outperforming other carbon-based fibers (table S1) (*7*, *20*, *21*). Therefore, this hybrid fiber can be a reliable basic component in next-generation fiber-based energy storage systems.

Nanosized zeolitic imidazolate frameworks were initially explored to develop hybrid composites with nanocarbons, including CNT and graphene. Previously, studies have reported that these small-sized metal-organic crystals are well incorporated into both the surface of nanocarbons and the gap between the nanocarbon aggregates, under carefully controlled reaction conditions (*22*–*24*). However, there have been no experimental approaches that offer a rapid, single-step synthesis to hybridize crystalline MOF onto the surface of CNTYs at a commercially viable scale to date. Given that various MOFs are constructed on these manifold substrates through heteronucleation (*14*–*16*), direct hydrothermal synthesis was performed, wherein the IRMOF-1 along with DWNTY were immersed in a precursor solution of zinc nitrate tetrahydrate and terephthalic acid. This synthesis method yielded a new class of "jeweled necklace"–like hybrid composite, wherein DWNTYs and IRMOF-1s comprised the chain and the beads, respectively (Fig. 2, A and C, and fig. S3). The submillimeter scale of the resulting products confirmed the successful growth of the framework on DWNTY substrate through heteronucleation. Notably, the overall cubic morphology with sharp facets was preserved with even the micrometer-thick fibers penetrating up to the middle of the framework. Typically, MOF synthesis in the presence of nanomaterials, such as biomacromolecules and carbon nanomaterials, yields an MOF crystal that retains the original cubic morphology after encapsulating the nanomaterials. Therefore, our results demonstrate the expanded availability of the substrate, allowing MOF growth on both curved and flexible surfaces.

Direct carbonization of hybrid composite, up to 900°C, endowed it with superior electrical conductivity and microporosity. Zn-based MOFs can be easily carbonized while retaining their original morphology. In addition, Zn species in hybrid composite fiber can be removed by carbothermal reduction during carbonization without subsequent etching process (*25*, *26*). As shown in Fig. 1A, heat treatment at 900°C expectedly transformed transparent MOFs into black-colored carbon. The OM and SEM images confirm thermal conversion of hybrid composite, wherein MDC beads attached onto DWNTY chain without failure (Fig. 2, B and D, and fig. S4). Raman spectroscopy further confirmed the formation of high crystalline IRMOF-1 on the curved surface of DWNTY (Fig. 2E). After thermal

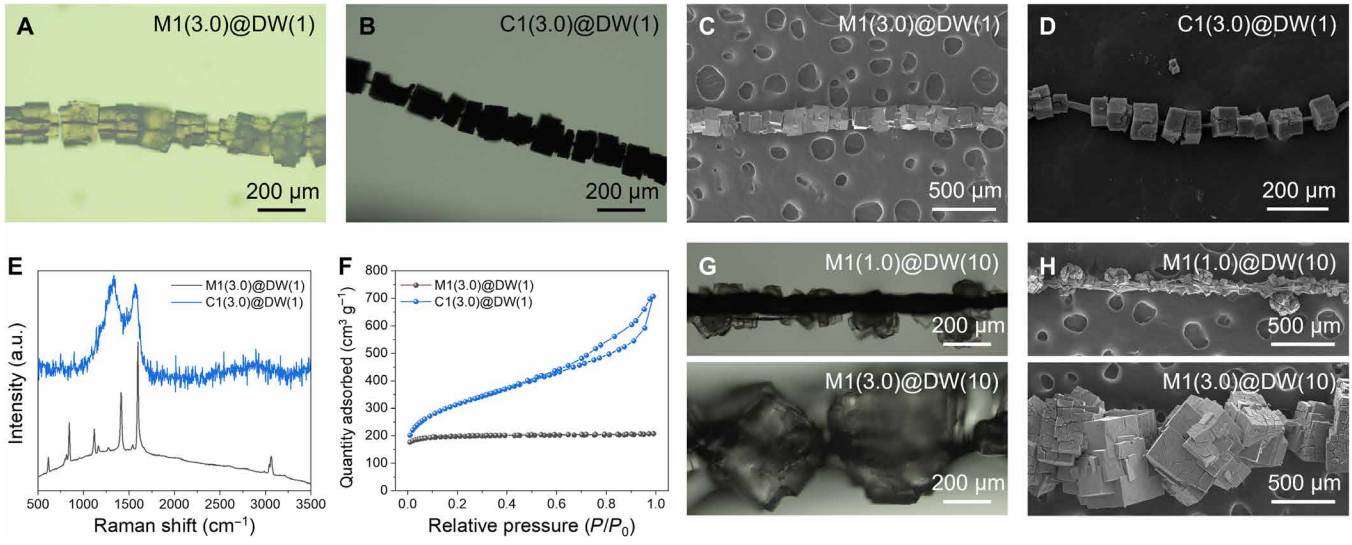

Fig. 2. Characterization of IRMOF-1@DWNTY and MDC-1@DWNTY. (**A** and **B**) OM images, (**C** and **D**) SEM images, (**E**) Raman spectra, and (**F**) N_2 sorption isotherms of M1(3.0)@DW(1) and C1(3.0)@DW(1). (**G**) OM images and (**H**) SEM images of M1@DW(10) at different precursor concentrations.

conversion, broad spectral bands representing the D (1334 cm^{-1}) and G (1567 cm^{-1}) bands of carbons indicated both complete carbonization and high porosity of the resulting carbons. Cryogenic N_2 sorption of the carbonized hybrid composites revealed combined characteristics of type I and type IV isotherms, wherein a steep increase was observed at low relative pressures, followed by a moderate increase at intermediate relative pressures accompanied by a desorption hysteresis (Fig. 2F). This highlights the formation of a hierarchical pore architecture comprising micro- and mesopores, which are mainly attributed to MDCs. The SSAs calculated on the basis of the Brunauer-Emmett-Teller equation were 785.8 and 1069.4 $m^2\ g^{-1}$ for IRMOF-1@DWNTY and MDC-1@DWNTY, respectively. These results demonstrated that nonporous DWNTY (SSA, 95.3 $m^2\ g^{-1}$) can be transformed into a highly porous hybrid fiber through the decoration of MDCs on its surface. Therefore, the proposed strategy can yield an extraordinary hybrid composite system that integrates two characteristics, high mechanical strength and high porosity, which are generally incompatible.

The versatility of this approach was further explored by controlling the thickness of DWNTY and the density of MOFs on DWNTY surface through modulation of precursor concentration. OM and SEM images revealed that density of MOFs can be easily controlled by modulating the precursor concentration, transforming smaller-sized MOFs into bigger-sized MOFs to cover the surface of 10 plies of the DWNTY fiber (Fig. 2, G and H, and fig. S5). These results demonstrate that loading amount of MOF on the curved surface can be customized by tuning synthesis conditions. We also monitored the structural changes under repetitive bending conditions to investigate the availability of this hybrid composite as an energy storage fiber under mechanical deformation. SEM images of C1(3.0)@DW(1) reveal some loss of MDCs after 2000 cycles of bending tests with a bending radius of 1 mm (fig. S6). Detachment of MDCs demonstrates that the interfacial strength of hybrid composite is not high enough to tolerate intensive mechanical stimulus and eventually causes overall performance degradation during the actual operation.

Controlling the interface of hybrid composite for high deformability

To promote stronger interfacial interaction in hybrid composite, we introduced functional groups onto both the surface of DWNTY and changed ligand used in MOF synthesis, thereby inducing additional intermolecular interactions (Fig. 3A). As shown in x-ray photoemission spectroscopy (XPS; Fig. 3B and figs. S7 and S8) and Fourier transform infrared (FT-IR; Fig. 3C) spectra, carboxylic groups were introduced on the surface of DWNTY via diazotization using *p*-aminobenzoic acid while maintaining original properties of DWNTY (table S2, denoted as mDWNTY) (*27*–*29*). X-ray diffraction (XRD) patterns also confirmed that diazotization functionalized the surface of DWNTY without change in graphitic structure (fig. S9). Furthermore, organic ligand was replaced with a ligand containing amine groups (IRMOF-3) to induce additional interactions with the newly introduced carboxylic group on the DWNTY surface. The synthesized IRMOF-3@mDWNTY showed yellowish crystals surrounding the DWNTY surface (Fig. 3, D and E). The color originates from the amine groups in the organic ligand, which is in agreement with the typical color of IRMOF-3 crystal (*30*, *31*). This demonstrates a viable strategy to incorporate bulky MOF crystals on the CNTY surface, regardless of organic ligands.

To validate the effect of the interface modifications on interfacial strength, we quantified the interfacial shear strength (IFSS) between DWNTYs and MOFs (Fig. 4A). In general, this method can be used to measure the IFSS between a fiber and a microdroplet of matrix (*29*). In an effort to mimic the system, we attempted to fabricate a hybrid composite of DWNTYs covered with one big MOF particle through limited immersion of DWNTs into an MOF precursor solution during crystallization, (Fig. 4, B and C, and movies S1 and S2), thereby adjusting the equation to calculate IFSS to our system. The IFSS value can be determined using the following equation, which is based on the assumption of a constant IFSS between DWNTYs and their surrounding MOFs

$$\mathrm{IFSS} = \frac{F}{\pi \times d \times L}$$

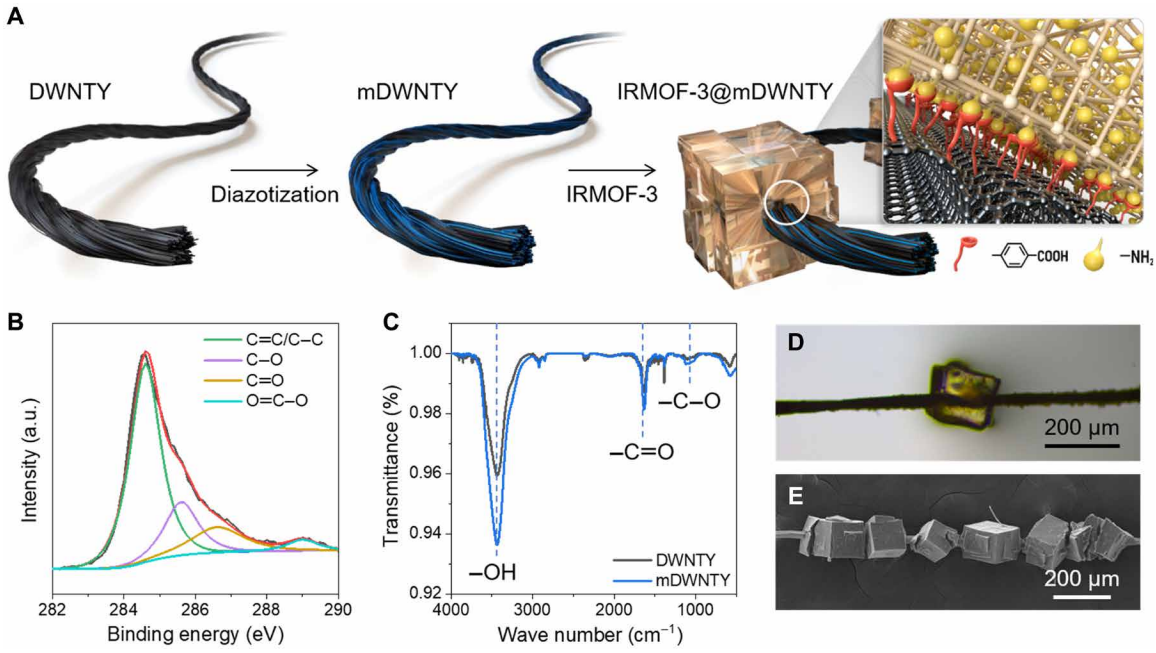

Fig. 3. Synthesis and characterization of IRMOF-3@mDWNTY. (**A**) Schematics illustrating the synthesis process to fabricate IRMOF-3@mDWNTY. (**B**) XPS C 1s spectrum and (**C**) FT-IR spectrum of mDWNTY. (**D**) OM image and (**E**) SEM image of IRMOF-3@mDWNTY.

where *F* is the maximum fiber axial force recorded at the onset of MOFs debonding (in newtons), *d* is the diameter of the DWNTYs (in meters), and *L* is the embedding length of the MOFs (in meters). The calculated IFSS value increased by 270% from 1.32 MPa for bare hybrid composites to 4.88 MPa for interface-controlled hybrid composites (Fig. 4D). These results indicate that the interfacial modifications were effective; therefore, we expected the detrimental segregation after several thousand bending tests to be alleviated.

Growth of IRMOF-3 on thickened mDWNTYs to enhance energy storage capability

Given that previous fiber-type energy storage systems required various additives, which can hamper their overall energy storage performance, we hypothesized that the storage performance can be maximized without deterioration by unnecessary additives upon fabrication of thickened fibers completely covered with porous materials. Therefore, to materialize this proposed design, we thickened mDWNTY by combining hundred fibers [denoted as mDW(100)] and then grew IRMOF-3 crystals on mDW(100) using controlled concentrations of precursor solutions, according to the aforementioned method (Fig. 5A). Hybrid composite fibers were denoted as M3(concentration)@mDW(100) and C3(concentration)@mDW(100) for IRMOF-3 and MDC-3, respectively. Physical and mechanical properties of hybrid composite fiber were summarized in table S3. On the basis of the change in tex, loading amount of MDC-3 on mDW(100) increased according to precursor concentration (fig. S10). OM and SEM images shown in Fig. 5B and fig. S11 display that the proposed structure was synthesized through heteronucleation. According to the thickness of mDWNTYs and precursor concentration, IRMOF-3 crystals compactly surrounded mDWNTYs, thereby achieving an unusually dense growth of MOF crystals on the substrate. Subsequent carbonization of IRMOF-3 crystals yielded conductive microporous carbons on the fibers without cracking or detachment (Fig. 5, C and D). After carbonization, XRD pattern of C3(1.0)@mDW(100) showed characteristic carbon (002) peak, while characteristic peaks of IRMOF-3 vanished (fig. S12). In addition, elemental maps of C3(1.0)@mDW(100) clarified that Zn species were removed by carbothermal reduction during carbonization (fig. S13). The IRMOF-3–derived carbon shrank along the fiber axis during carbonization, generating space between MDCs. This morphology is presumed to be ideal for flexible motions such as bending, folding, and twisting of the yarn because the space between MDCs relieves friction between them. Considering that yarns are expected to withstand various deformations during textile processing (*32*, *33*), the morphological features of C3@mDW(100) are appropriate to design fiber and textile supercapacitors. Raman spectra of C3@mDW(100) at different concentrations exhibited broad bands of *D* and *G* bands of carbons, confirming the complete carbonization of IRMOF-3 (Fig. 5E). Moreover, N_2 sorption isotherms demonstrated hierarchical pore architecture in the carbonized hybrid composites with high SSA (Fig. 5F).

Furthermore, we measured the mechanical properties of hybrid composites because the internal and external structures of the inherent DWNTs can be hampered during synthesis, involving crystal growth and heating at high temperatures. As shown in Fig. 5G, C3@mDW(100) synthesized using different precursor concentrations can withstand high tensile loads before breaking, almost equivalent to that handled by mDW(100), reconfirming that the mechanical robustness was well preserved without breakdown of internal and external structures of DWNTYs. The tensile strength values of C3@mDW(100) further highlight the mechanical robustness of the fibers (table S3). C3(1.0)@mDW(100) exhibited markedly high tensile strength (492.8 MPa), suggesting that the C3@mDW(100)-based supercapacitor can be used in multifunctional devices requiring

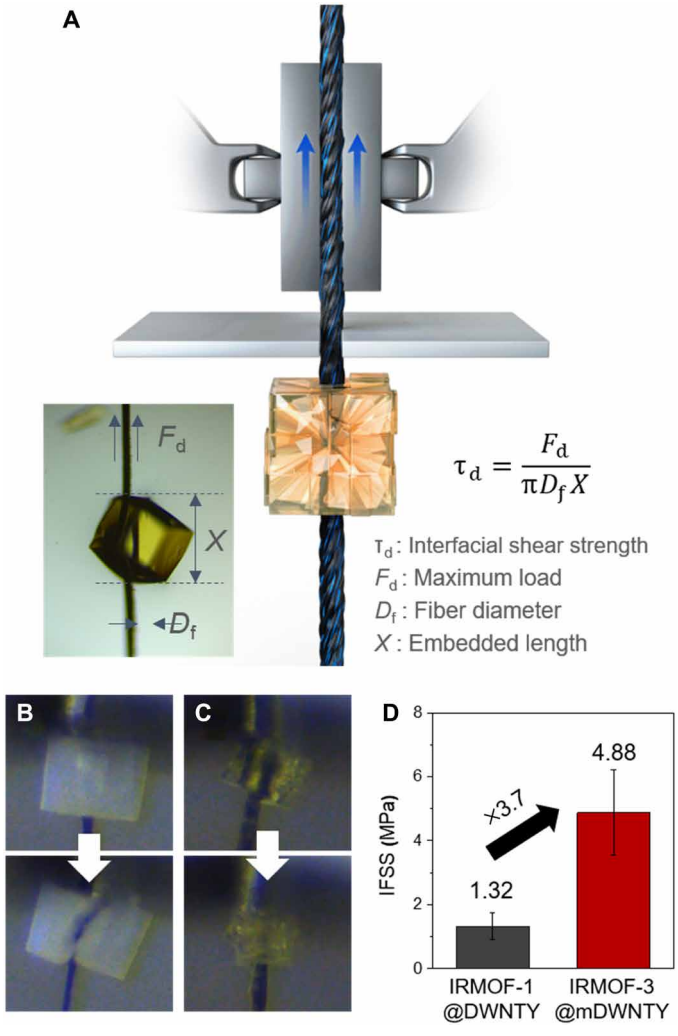

Fig. 4. IFSS measurement of hybrid composite fibers. (**A**) Schematic illustrating IFSS measurement of IRMOF-3@mDWNTY. Optical images of (**B**) IRMOF-1@DWNTY and (**C**) IRMOF-3@mDWNTY during IFSS measurement. (**D**) Comparison of measured IFSS values.

both superior mechanical properties and energy storage performance, simultaneously. The tensile strength of C3(1.0)@mDW(100) is even higher than that of most pure metals. C3(1.5) and C3(2.0)@mDW(100) also exhibited high tensile strengths (445.3 and 380.2 MPa, respectively), even after incorporating a large amount of MDCs on mDWNTYs. We further measured the resistance of C3(1.0)@mDW(100) after being subjected to more than 5000 cycles of repetitive bending using automatic bending machine (fig. S14). Original structure of hybrid composite fiber was preserved even after 5000 bending cycles (fig. S15). Moreover, relative resistance was maintained constant, elucidating that electrical pathway network was undisrupted even after repetitive bending (Fig. 5H). These results demonstrated superior mechanical properties of these hybrid composite fibers.

Energy storage performances of MDC-3@mDWNTY were evaluated by cyclic voltammetry (CV) and galvanostatic charge-discharge (GCD) measurements using an all-solid-state supercapacitor comprising C3@mDW(100) in a symmetric two-electrode configuration with gel electrolyte. The all-solid-state supercapacitor exhibited high flexibility similar to original C3@mDW(100), as demonstrated by no structural deterioration even in a twisted state (Fig. 6A). CV (Fig. 6B and fig. S16) and GCD curves (Fig. 6C and fig. S17) of all C3@mDW(100)-based supercapacitors had quasi-rectangular and symmetric triangular shapes, respectively, confirming the ideal electrical double layer capacitance (EDLC) behavior of the fiber-type supercapacitors prepared in this work (*34*). Only small voltage drops (<0.05 V) were observed in the GCD measurements of all-solid-state supercapacitors, which guarantees proper device operation for high discharge rates (1 A g^{-1}). Furthermore, the C3@mDW(100)-based supercapacitors exhibited almost equivalent electrochemical behavior, regardless of the electrolyte type (liquid or gel) (figs. S18 and S19). These results validate the exceptional electrolyte accessibility of C3@mDW(100), enabling the feasible operation of the all-solid-state supercapacitor.

Gravimetric, volumetric, and length capacitances of the C3@mDW(100)-based all-solid-sate supercapacitors were determined using GCD measurements (Fig. 6, D and E, and fig. S20). Gravimetric and volumetric capacitances were calculated on the basis of the total electrode mass and volume, respectively. Capacitances of all devices were higher than 200 F cm^{-3}, which is a remarkably high value, considering all electrodes contained only carbon-based materials without any other pseudo-capacitive materials. Higher amounts of MDC-3 on DWNTY increase the length and volumetric capacitances while decreasing gravimetric capacitance. Although C3(2.0)@mDW(100) had the highest SSA, it exhibited the lowest gravimetric capacitance (138.9 F g^{-1}) compared to those of C3(1.5)@mDW(100) (145.0 F g^{-1}) and C3(1.0)@mDW(100) (151.1 F g^{-1}). Large amounts of MDC-3 also deteriorated rate capability of the supercapacitors. As shown in the Nyquist plots of the supercapacitors (fig. S21), mDW(100) and C3(1.0)@mDW(100) showed almost identical plots, indicating that connection between DWNTY and MDC-3 did not increase series resistance. It was confirmed that resistance increased as IRMOF-3 grew larger depending on precursor concentration. This is because distance increased between MDC-3 providing charge storable sites and DWNTY, ensuring conductive pathway. The capacitance of C3(2.0)@mDW(100) decreased from 253.3 to 204.0 F cm^{-3} (80.5% retention) when current density was increased from 0.5 to 4.0 A g^{-1}, whereas C3(1.0)@mDW(100) exhibited an exceptional capacitance retention of 94%.

Cycle stability of the supercapacitor was characterized by GCD tests at 1.0 A g^{-1}. The C3(1.0)@mDW(100)-based all-solid-state supercapacitor had a capacitance retention of 87.4% after 500 charge-discharge cycles (Fig. 6F). Notably, the C3(1.0)@mDW(100)-based supercapacitor achieved stable cycle performance with a retention of 88.9% after 10,000 cycles, when an aqueous electrolyte was used (fig. S22). Therefore, these results confirmed that capacitance degradation was predominantly caused by evaporation of the solvent in the gel electrolyte rather than the structural deterioration of fiber electrodes.

Volumetric energy and power densities of representative fiber-type EDLCs are shown in a Ragone plot (Fig. 6G) (*35*–*46*). The C3(1.0)@mDW(100)-based all-solid-state supercapacitor fabricated in this study evidently exhibited the highest energy and power densities among reported fiber-type EDLCs. The Ragone plot proves that combining highly conductive DWNTY and microporous MDC is the ideal strategy to prepare fiber-type supercapacitors with high energy storage performances. The tensile strength of the electrode and volumetric capacitance of fiber-type supercapacitors were

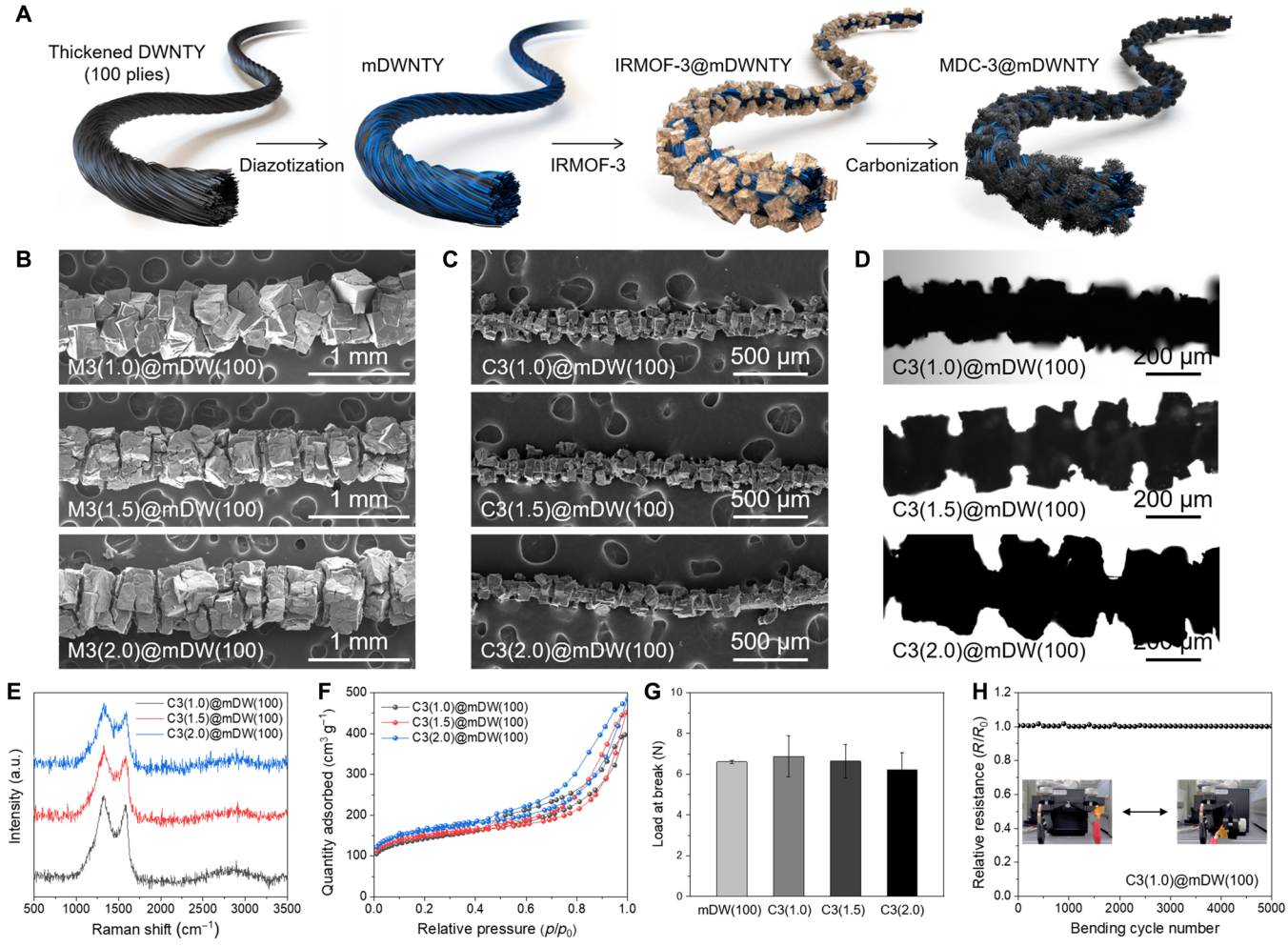

Fig. 5. Synthesis and characterization of thickened MDC-3@mDWNTY. (**A**) Schematics illustrating the synthesis process to prepare thickened M3@mDW(100). (**B**) SEM images of M3@mDW(100) at different precursor concentrations. (**C**) SEM images, (**D**) OM images, (**E**) Raman spectra, (**F**) N_2 sorption isotherms, and (**G**) load at break of C3@mDW(100) at different precursor concentrations. (**H**) Relative resistance of C3(1.0)@mDW(100) during repetitive bending.

compared with those reported in recent studies (Fig. 6H); the details of these studies are shown in table S4 (*42*, *43*, *47*–*56*). The fiber-type supercapacitors based on C3@mDW(100) concurrently deliver the highest volumetric energy density and tensile strength. Most studies have reported electrode tensile strengths of less than 200 MPa, indicating the superior mechanical strength of C3@mDW(100). Moreover, note that capacitance of our supercapacitors is even higher than the benchmark for fiber-type pseudo-capacitors.

Energy storage performance of the hybrid composite–based all-solid-state supercapacitor under extreme conditions

The mechanical robustness of the C3(1.0)@mDW(100)-based all-solid-state supercapacitors was confirmed through demonstrations of cycle stability of the fiber-type supercapacitors under various deformation conditions. Even after repeated bending every 100 charge-discharge cycles, the C3(1.0)@mDW(100)-based supercapacitor had a capacitance retention of 88.0% after 500 cycles, which is almost the same as that without mechanical deformation; this validates the superior flexibility of the fiber-type supercapacitor (Fig. 7A). Furthermore, note that the energy storage performance did not deteriorate notably at any of the various bending angles (Fig. 7B). The capacitance reduced when the fiber-type supercapacitor was knotted; however, the capacitance was regained upon recovery of the deformation. We further confirmed that the capacitance retention increased to 100% when the evaporated solvent in the gel electrolyte was replenished with an aqueous H_3PO_4 solution. These results demonstrate the mechanical reliability of the supercapacitor for fiber processing technology.

Some articles have reported that fiber-type electrodes for supercapacitors can hold hundreds of grams to demonstrate mechanical robustness (*49*, *56*–*58*). However, to our knowledge, there have been no reports of fiber-type supercapacitor being operating while supporting a load. This study demonstrates a superstrong supercapacitor that can simultaneously turn on an LED light while supporting a 10-kg weight. Because the voltage required to turn on red LED light is higher than 1 V (1.8 V), we used polyvinyl alcohol–dimethyl sulfoxide (PVA-DMSO) gel electrolyte instead of PVA hydrogel electrolyte to enlarge the voltage window of the supercapacitor. Figure 7C displays CV curves of the all-solid-state supercapacitor based on C3(3.0)@mDW(2000) with PVA-DMSO gel.

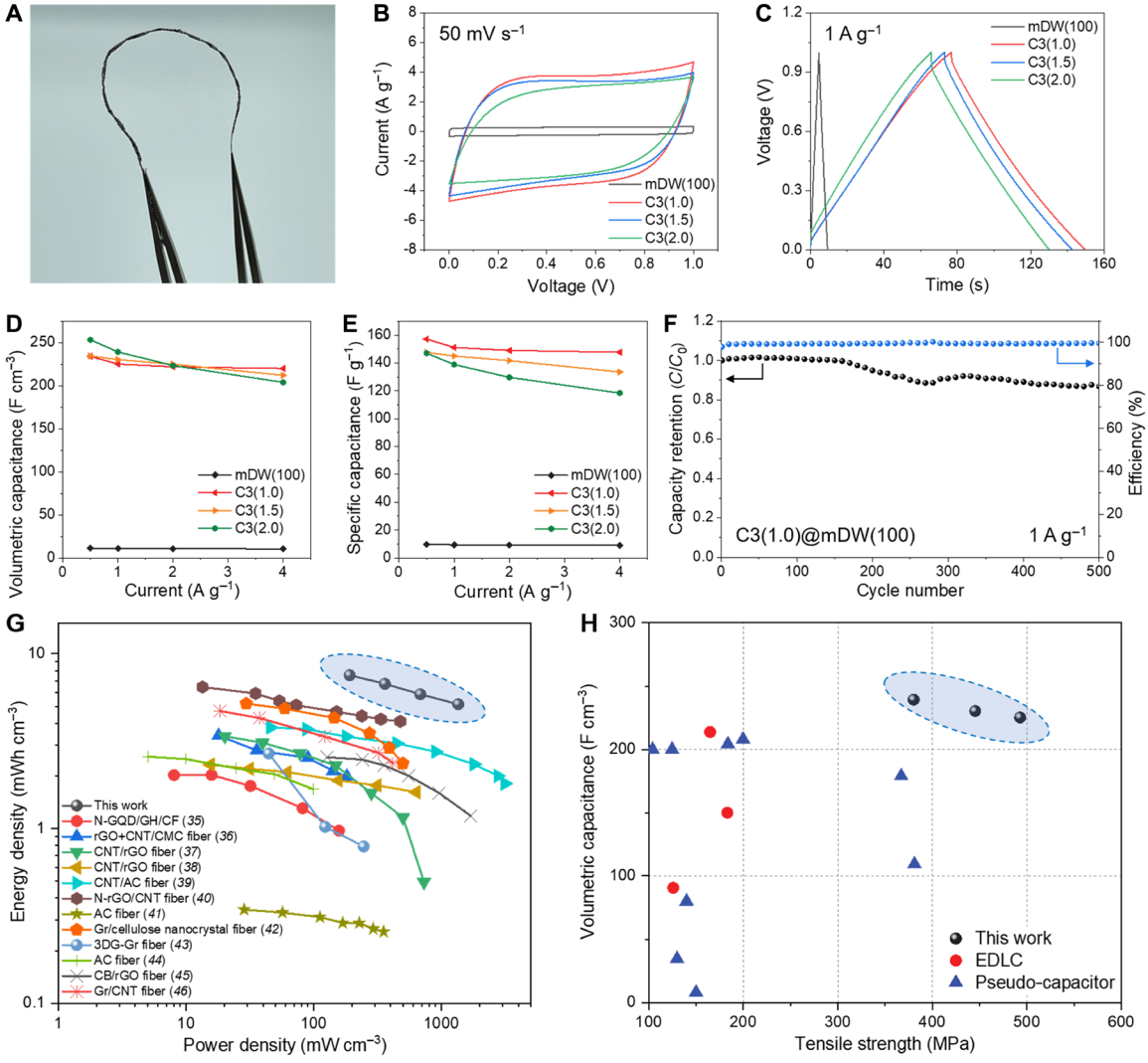

Fig. 6. Energy storage performances of the MDC-3@mDWNTY-based all-solid-state supercapacitor. (**A**) Digital photograph of the C3@mDW(100)-based all-solid-state supercapacitor. (**B**) CV curves at 50 mV s^{-1}, (**C**) GCD profile at 1 A g^{-1}, (**D**) volumetric capacitance, and (**E**) specific capacitance of the prepared supercapacitors. (**F**) Cycle performance of the C3(1.0)@mDW(100)-based supercapacitor at 1 A g^{-1}. (**G**) Ragone plots comparing our data with recently reported fiber-type EDLCs. (**H**) Ashby plots of volumetric capacitance and tensile strength for the state-of-the-art fiber-type supercapacitors.

The quasi-rectangular shape of CV curves confirmed the EDLC behavior of the supercapacitor. Moreover, 2.7 V can be properly charged and discharged in a single fiber-type supercapacitor, indicating that it can switch on the LED by itself without requiring serial connection of multiple devices. The fiber-type supercapacitor was tied into a fisherman's knot to hold the weight. As shown in Fig. 7D, the knotted supercapacitor can turn on red LED light while supporting a 10-kg plate without malfunctioning. These results elucidate that the proposed strategy realizes to integrate all crucial characteristics, superior mechanical robustness, and stable electrochemical reliability into one fiber functioning as a supercapacitor electrode that is applicable to wearable devices and stable in extreme operating environments.

DISCUSSION

In conclusion, we demonstrated a new class of jeweled necklace–like hybrid composite fiber comprising DWNTY coated with MOF beads as an all-in-one fiber-type all-solid-state supercapacitor. Interfacial interaction between MOF and DWNTY was controlled by surface modification of DWNTY through diazotization and ligand selection. MOF beads were thermally converted into microporous MDCs, thereby maximizing energy storage capability while maintaining robust mechanical properties of DWNTY. Furthermore, the thickness and MDC loading amount of hybrid fiber can be easily controlled to fit desired dimensions. The resulting hybrid composite fiber delivered high volumetric capacitance (225.2 F cm^{-3}) and specific capacitance (151.1 F g^{-1}) at 1 A g^{-1} with exceptional tensile strength (492.8 MPa). The mechanical robustness of the C3(1.0)@mDW(100)-based supercapacitors was confirmed by demonstrating stable cycle performance under various mechanical deformation conditions, including cumulative repetitive bending and various bending angles. Furthermore, the hybrid fiber supercapacitor can stably operate to switch on an LED light even under the extreme condition of suspending a 10-kg plate, highlighting its outstanding

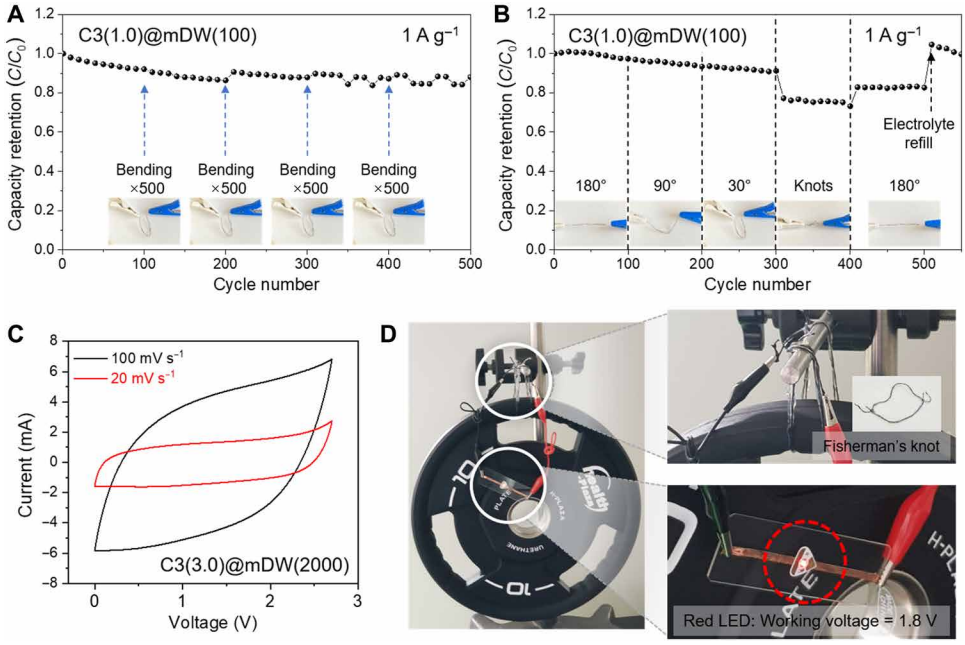

Fig. 7. Electrochemical and mechanical reliability of MDC-3@mDWNTY-based all-solid-state supercapacitor under various deformation conditions. Cycle performance of the C3(1.0)@mDW(100)-based all-solid-state supercapacitor under (**A**) cumulative bending and (**B**) at different bending angles at 1 A g^{-1}. (**C**) CV curves of the C3(3.0)@mDW(2000)-based all-solid-state supercapacitor. (**D**) Practical demonstration of the all-solid-state fiber-type supercapacitor under extreme conditions, suspending a 10-kg plate.

mechanical robustness and flexibility. This study establishes a straightforward strategy to prepare hybrid composite fibers that endow mechanical robustness and energy storage reliability to high-performance fiber-type supercapacitors.

MATERIALS AND METHODS

Synthesis of DWNTY

DWNTY was synthesized by continuous direct spinning in a vertical furnace at 1200°C (*28*, *29*, *59*, *60*). Ferrocene, thiophene, methane, and hydrogen gas were used as the catalyst, promotor, carbon source, and carrier gas, respectively. Before synthesizing DWNTY, the vertical furnace was purged with high purity Ar (99.999%) for 10 min, and the atmosphere was changed by adding hydrogen (99.999%) just before synthesis. Subsequently, methane, ferrocene, and thiophene were added into the vertical furnace, and DWNT aerogel was produced at the bottom of the reactor. DWNT aerogel was passed at constant rate through a water bath to yield DWNTY. Thickened DWNTY was manufactured by twisting the yarns and integrating them into one fiber.

Surface modification of DWNTY

Diazotization was used to introduce carboxyl groups on the DWNTY. First, DWNTY was immersed into a solution comprising 1.0972 g of *p*-aminobenzoic acid dissolved in 113.3 ml of 1 M HCl. Then, 0.5521 g of sodium nitrate ($NaNO_2$) was dissolved in 46.7 ml of 1 M HCl solution and poured into the first solution. Subsequently, the reaction proceeded at 70°C for 24 hours. Upon completion of the reaction, the surface-modified DWNTY was washed several times with acetone and dimethylformamide (DMF).

MOF growth on DWNTY

For IRMOF-1@DWNTY, 0.784 g of zinc nitrate tetrahydrate (3 mmol), 0.166 g of terephthalic acid (1 mmol), and DWNTY were dissolved in DMF (30 ml) in a Teflon-lined autoclave. The reaction mixture was heated in a convection oven at 105°C for 24 hours to synthesize IRMOF-1 on DWNTY. The mixture was removed from the oven and allowed to cool to room temperature. The resulting IRMOF-1@DWNTY was washed with DMF, immersed in anhydrous chloroform for 3 hours, and vacuum-dried at 150°C overnight. For IRMOF-3@mDWNTY, 0.784 g of zinc nitrate tetrahydrate (3 mmol), 0.181 g of 2-aminoterephthalic acid (1 mmol), and mDWNTY were dissolved in DMF (30 ml) in a Teflon-lined autoclave. The subsequent steps were same as those described for IRMOF-1@DWNTY.

Thermal conversion of hybrid composite fiber

The prepared hybrid composite fibers were transferred to a tube furnace and heat-treated at 900°C under nitrogen atmosphere with a heating rate of 5°C min^{-1}. After reaching the target temperature, the materials were maintained at 900°C for 3 hours and then cooled to room temperature.

Characterization

The structure of hybrid composite fibers was investigated using OM (DM750M, Leica), SEM (S-4300SE, Hitachi), and TEM (JEM-2100F, JEOL). Raman spectroscopy was performed using a RAMANplus confocal laser Raman microscope (Nanophoton) for physicochemical surface analysis. Nitrogen adsorption isotherms at liquid nitrogen temperature (77 K) were conducted using a SSA meter (TriStar 2, Micromeritics). Chemical bonding on the surface of DWNTY was investigated using x-ray photoelectron spectroscopy (K-Alpha,

Thermo Fisher Scientific) and FT-IR (VERTEX 80V, Bruker) analysis. TGA was performed under an air flow with a heating rate of 5°C min^{-1}, using a TGA-N1000 (Scinco). Tensile strength and IFSS were measured using the universal tensile machine (Instron 3344, Instron) at tensile rates of 2 and 0.5 mm min^{-1}, respectively.

Electrochemical measurements

Gel-type electrolyte was prepared by mixing 1 g of PVA (M_w = 86,000) and 10 ml of 1.5 M H_3PO_4 solution and stirring at 80°C for 2 hours until PVA was dissolved. For extreme condition test, gel-type electrolyte was prepared by mixing 1 g of PVA (M_w = 136,000), 1.06 g of $LiClO_4$, and 10 ml of DMSO. As-prepared gel-type electrolyte was coated on the surface of C3@mDW(100), followed by immersing in methanol for 30 s for curing. Electrolyte coating was repeated four to five times to achieve uniform coating (fig. S23). Then, two identical electrolyte-coated C3@mDW(100) electrodes were twisted and attached by additional curing of a small amount of electrolyte in the gap between the electrodes. Electrochemical characterizations were conducted using a potentiostat (VSP-300, Biologic) in a symmetric two-electrode configuration. The single electrode capacitance of the fiber supercapacitors was calculated from GCD curves using the equation

$$\text{Specific capacitance } C_S = 2 \times \frac{I\Delta t}{m\Delta V}$$

$$\text{Volumetric capacitance } C_V = \frac{C_S}{d}$$

$$\text{Length capacitance } C_L = \frac{mC_S}{L}$$

where m is the mass of single electrode, L is the length of fiber supercapacitor, and d is the density of single electrode. Density was measured using balance (XPE205V, Mettler Toledo) with density accessory kit based on Archimedes' principle. Density of the sample (ρ) can be calculated as follows

$$\rho = \frac{W_0}{W_0 - W_L}(\rho_L - \rho_0) + \rho_0$$

where ρ, ρ_0, and ρ_L are density of the sample, air, and liquid, respectively, and W_0 and W_L represent weight of the sample in the air and liquid, respectively. The energy and power densities of the full cell were calculated according to the formula

$$\text{Volumetric energy density } E_V = \frac{1}{8} C_V V^2 \times \frac{1}{3600}$$

$$\text{Volumetric power density } P_V = \frac{E_V}{t}$$

SUPPLEMENTARY MATERIALS

Supplementary material for this article is available at https://science.org/doi/10.1126/sciadv.abl8631

REFERENCES AND NOTES

1. E. Pomerantseva, F. Bonaccorso, X. Feng, Y. Cui, Y. Gogotsi, Energy storage: The future enabled by nanomaterials. *Science* **366**, eaan8285 (2019).
2. Y. Zhang, J. He, Z. Gao, X. Li, Converting eggs to flexible, all-solid supercapacitors. *Nano Energy* **65**, 104045 (2019).
3. Z. Gao, C. Bumgardner, N. Song, Y. Zhang, J. Li, X. Li, Cotton-textile-enabled flexible self-sustaining power packs via roll-to-roll fabrication. *Nat. Commun.* **7**, 11586 (2016).
4. L. Bao, J. Zang, X. Li, Flexible Zn2SnO4/MnO2 core/shell nanocable–carbon microfiber hybrid composites for high-performance supercapacitor electrodes. *Nano Lett.* **11**, 1215–1220 (2011).
5. X. Lu, M. Yu, G. Wang, Y. Tong, Y. Li, Flexible solid-state supercapacitors: Design, fabrication and applications. *Energy Environ. Sci.* **7**, 2160–2181 (2014).
6. Z. Gao, W. Yang, J. Wang, N. Song, X. Li, Flexible all-solid-state hierarchical $NiCo_2O_4$/porous graphene paper asymmetric supercapacitors with an exceptional combination of electrochemical properties. *Nano Energy* **13**, 306–317 (2015).
7. G. Xin, T. Yao, H. Sun, S. M. Scott, D. Shao, G. Wang, J. Lian, Highly thermally conductive and mechanically strong graphene fibers. *Science* **349**, 1083–1087 (2015).
8. F. Bonaccorso, L. Colombo, G. Yu, M. Stoller, V. Tozzini, A. C. Ferrari, R. S. Ruoff, V. Pellegrini, Graphene, related two-dimensional crystals, and hybrid systems for energy conversion and storage. *Science* **347**, 1246501 (2015).
9. Y. Li, J. Zhang, Q. Chen, X. Xia, M. Chen, Emerging of heterostructure materials in energy storage: A review. *Adv. Mater.* **33**, 2100855 (2021).
10. Z. Gao, Y. Zhang, N. Song, X. Li, Biomass-derived renewable carbon materials for electrochemical energy storage. *Mater. Res. Lett.* **5**, 69–88 (2017).
11. Z. Gao, N. Song, Y. Zhang, Y. Schwab, J. He, X. Li, Carbon nanotubes derived from yeast-fermented wheat flour and their energy storage application. *ACS Sustain. Chem. Eng.* **6**, 11386–11396 (2018).
12. C. Wang, K. Xia, H. Wang, X. Liang, Z. Yin, Y. Zhang, Advanced carbon for flexible and wearable electronics. *Adv. Mater.* **31**, 1801072 (2019).
13. Y. Jang, S. M. Kim, G. M. Spinks, S. J. Kim, Carbon nanotube yarn for fiber-shaped electrical sensors, actuators, and energy storage for smart systems. *Adv. Mater.* **32**, 1902670 (2020).
14. C. M. Doherty, D. Buso, A. J. Hill, S. Furukawa, S. Kitagawa, P. Falcaro, Using functional nano- and microparticles for the preparation of metal–organic framework composites with novel properties. *Acc. Chem. Res.* **47**, 396–405 (2014).
15. P. Falcaro, K. Okada, T. Hara, K. Ikigaki, Y. Tokudome, A. W. Thornton, A. J. Hill, T. Williams, C. Doonan, M. Takahashi, Centimetre-scale micropore alignment in oriented polycrystalline metal–organic framework films via heteroepitaxial growth. *Nat. Mater.* **16**, 342–348 (2017).
16. A. Tarzia, M. Takahashi, P. Falcaro, A. W. Thornton, C. J. Doonan, D. M. Huang, High-throughput screening of metal–organic frameworks for macroscale heteroepitaxial alignment. *ACS Appl. Mater. Interfaces* **10**, 40938–40950 (2018).
17. S. J. Yang, T. Kim, J. H. Im, Y. S. Kim, K. Lee, H. Jung, C. R. Park, MOF-derived hierarchically porous carbon with exceptional porosity and hydrogen storage capacity. *Chem. Mater.* **24**, 464–470 (2012).
18. J. Lee, D.-M. Lee, Y. Jung, J. Park, H. S. Lee, Y.-K. Kim, C. R. Park, H. S. Jeong, S. M. Kim, Direct spinning and densification method for high-performance carbon nanotube fibers. *Nat. Commun.* **10**, 2962 (2019).
19. G. Leofanti, M. Padovan, G. Tozzola, B. Venturelli, Surface area and pore texture of catalysts. *Catal. Today* **41**, 207–219 (1998).
20. Z. Zhang, W. Yang, L. Cheng, W. Cao, M. Sain, J. Tan, A. Wang, H. Jia, Carbon fibers with high electrical conductivity: Laser irradiation of mesophase pitch filaments obtains high graphitization degree. *ACS Sustain. Chem. Eng.* **8**, 17629–17638 (2020).
21. X. Xi, D. D. L. Chung, Colossal electric permittivity discovered in polyacrylonitrile (PAN) based carbon fiber, with comparison of PAN-based and pitch-based carbon fibers. *Carbon* **145**, 734–739 (2019).
22. W. Xia, C. Qu, Z. Liang, B. Zhao, S. Dai, B. Qiu, Y. Jiao, Q. Zhang, X. Huang, W. Guo, D. Dang, R. Zou, D. Xia, Q. Xu, M. Liu, High-performance energy storage and conversion materials derived from a single metal–organic framework/graphene aerogel composite. *Nano Lett.* **17**, 2788–2795 (2017).
23. H. Zhang, W. Zhao, Y. Wu, Y. Wang, M. Zou, A. Cao, Dense monolithic MOF and carbon nanotube hybrid with enhanced volumetric and areal capacities for lithium–sulfur battery. *J. Mater. Chem. A* **7**, 9195–9201 (2019).
24. J. Gu, L. Sun, Y. Zhang, Q. Zhang, X. Li, H. Si, Y. Shi, C. Sun, Y. Gong, Y. Zhang, MOF-derived Ni-doped CoP@C grown on CNTs for high-performance supercapacitors. *Chem. Eng. J.* **385**, 123454 (2020).
25. P. Strubel, S. Thieme, T. Biemelt, A. Helmer, M. Oschatz, J. Brückner, H. Althues, S. Kaskel, ZnO hard templating for synthesis of hierarchical porous carbons with tailored porosity and high performance in lithium-sulfur battery. *Adv. Funct. Mater.* **25**, 287–297 (2015).
26. J. Hwang, R. Walczak, M. Oschatz, N. V. Tarakina, B. V. K. J. Schmidt, Micro-blooming: Hierarchically porous nitrogen-doped carbon flowers derived from metal-organic mesocrystals. *Small* **15**, 1901986 (2019).
27. L. Cui, Y. Xu, B. Liu, W. Yang, Z. Song, J. Liu, Well-controlled preparation of evenly distributed nanoporous HOPG surface via diazonium salt assisted electrochemical etching process. *Carbon* **102**, 419–425 (2016).
28. J. Y. Cheon, N. Ku, Y. Jung, K. Lee, T. Kim, Hydrophilic treatment for strong carbon nanotube fibers. *Funct. Compos. Struct.* **3**, 025002 (2021).

29. T. Kim, J. Shin, K. Lee, Y. Jung, S. B. Lee, S. J. Yang, A universal surface modification method of carbon nanotube fibers with enhanced tensile strength. *Compos. Part A Appl. Sci. Manuf.* **140**, 106182 (2021).
30. J. L. C. Rowsell, O. M. Yaghi, Effects of functionalization, catenation, and variation of the metal oxide and organic linking units on the low-pressure hydrogen adsorption properties of metal–organic frameworks. *J. Am. Chem. Soc.* **128**, 1304–1315 (2006).
31. S. Rostamnia, H. Xin, Basic isoreticular metal–organic framework (IRMOF-3) porous nanomaterial as a suitable and green catalyst for selective unsymmetrical Hantzsch coupling reaction. *Appl. Organomet. Chem.* **28**, 359–363 (2014).
32. Y. Jung, Y. C. Jeong, J. H. Kim, Y. S. Kim, T. Kim, Y. S. Cho, S. J. Yang, C. R. Park, One step preparation and excellent performance of CNT yarn based flexible micro lithium ion batteries. *Energy Storage Mater.* **5**, 1–7 (2016).
33. J. Choi, Y. Jung, S. J. Yang, J. Y. Oh, J. Oh, K. Jo, J. G. Son, S. E. Moon, C. R. Park, H. Kim, Flexible and robust thermoelectric generators based on all-carbon nanotube yarn without metal electrodes. *ACS Nano* **11**, 7608–7614 (2017).
34. P. Simon, Y. Gogotsi, Materials for electrochemical capacitors. *Nat. Mater.* **7**, 845–854 (2008).
35. Z. Li, J. Wei, J. Ren, X. Wu, L. Wang, D. Pan, M. Wu, Hierarchical construction of high-performance all-carbon flexible fiber supercapacitors with graphene hydrogel and nitrogen-doped graphene quantum dots. *Carbon* **154**, 410–419 (2019).
36. L. Kou, T. Huang, B. Zheng, Y. Han, X. Zhao, K. Gopalsamy, H. Sun, C. Gao, Coaxial wet-spun yarn supercapacitors for high-energy density and safe wearable electronics. *Nat. Commun.* **5**, 3754 (2014).
37. Y. Ma, P. Li, J. W. Sedloff, X. Zhang, H. Zhang, J. Liu, Conductive graphene fibers for wire-shaped supercapacitors strengthened by unfunctionalized few-walled carbon nanotubes. *ACS Nano* **9**, 1352–1359 (2015).
38. B. Wang, X. Fang, H. Sun, S. He, J. Ren, Y. Zhang, H. Peng, Fabricating continuous supercapacitor fibers with high performances by integrating all building materials and steps into one process. *Adv. Mater.* **27**, 7854–7860 (2015).
39. Q. Meng, H. Wu, Y. Meng, K. Xie, Z. Wei, Z. Guo, High-performance all-carbon yarn micro-supercapacitor for an integrated energy system. *Adv. Mater.* **26**, 4100–4106 (2014).
40. D. Yu, K. Goh, H. Wang, L. Wei, W. Jiang, Q. Zhang, L. Dai, Y. Chen, Scalable synthesis of hierarchically structured carbon nanotube–graphene fibres for capacitive energy storage. *Nat. Nanotechnol.* **9**, 555–562 (2014).
41. D. Yu, S. Zhai, W. Jiang, K. Goh, L. Wei, X. Chen, R. Jiang, Y. Chen, Transforming pristine carbon fiber tows into high performance solid-state fiber supercapacitors. *Adv. Mater.* **27**, 4895–4901 (2015).
42. G. Chen, T. Chen, K. Hou, W. Ma, M. Tebyetekerwa, Y. Cheng, W. Weng, M. Zhu, Robust, hydrophilic graphene/cellulose nanocrystal fiber-based electrode with high capacitive performance and conductivity. *Carbon* **127**, 218–227 (2018).
43. S. W. Hasan, Z. Taha, Q. Meng, J. Shen, T. Lyu, J. Zhu, C. Li, Z. Q. Tian, P. K. Shen, Interstitial nanoclusters within graphene sheets for highly conductive, strong and electrochemically active fiber-shaped supercapacitors. *Appl. Mater. Today* **20**, 100768 (2020).
44. W. Ma, S. Chen, S. Yang, W. Chen, W. Weng, M. Zhu, Bottom-up fabrication of activated carbon fiber for all-solid-state supercapacitor with excellent electrochemical performance. *ACS Appl. Mater. Interfaces* **8**, 14622–14627 (2016).
45. W. Ma, S. Chen, S. Yang, M. Zhu, Hierarchically porous carbon black/graphene hybrid fibers for high performance flexible supercapacitors. *RSC Adv.* **6**, 50112–50118 (2016).
46. H. Park, R. B. Ambade, S. H. Noh, W. Eom, K. H. Koh, S. B. Ambade, W. J. Lee, S. H. Kim, T. H. Han, Porous graphene-carbon nanotube scaffolds for fiber supercapacitors. *ACS Appl. Mater. Interfaces* **11**, 9011–9022 (2019).
47. W. Jiang, S. Zhai, Q. Qian, Y. Yuan, H. E. Karahan, L. Wei, K. Goh, A. K. Ng, J. Wei, Y. Chen, Space-confined assembly of all-carbon hybrid fibers for capacitive energy storage: Realizing a built-to-order concept for micro-supercapacitors. *Energy Environ. Sci.* **9**, 611–622 (2016).
48. N. He, W. Shan, J. Wang, Q. Pan, J. Qu, G. Wang, W. Gao, Mordant inspired wet-spinning of graphene fibers for high performance flexible supercapacitors. *J. Mater. Chem. A* **7**, 6869–6876 (2019).
49. D. Liu, J. Liu, Q. Wang, P. Du, W. Wei, P. Liu, PANI coated microporous graphene fiber capable of subjecting to external mechanical deformation for high performance flexible supercapacitors. *Carbon* **143**, 147–153 (2019).
50. P. Shi, L. Li, L. Hua, Q. Qian, P. Wang, J. Zhou, G. Sun, W. Huang, Design of amorphous manganese oxide@multiwalled carbon nanotube fiber for robust solid-state supercapacitor. *ACS Nano* **11**, 444–452 (2017).
51. C. Choi, H. J. Sim, G. M. Spinks, X. Lepró, R. H. Baughman, S. J. Kim, Elastomeric and dynamic MnO_2/CNT core–shell structure coiled yarn supercapacitor. *Adv. Energy Mater.* **6**, 1502119 (2016).
52. J. A. Lee, M. K. Shin, S. H. Kim, H. U. Cho, G. M. Spinks, G. G. Wallace, M. D. Lima, X. Lepró, M. E. Kozlov, R. H. Baughman, S. J. Kim, Ultrafast charge and discharge biscrolled yarn supercapacitors for textiles and microdevices. *Nat. Commun.* **4**, 1970 (2013).
53. L. Hua, P. Shi, L. Li, C. Yu, R. Chen, Y. Gong, Z. Du, J. Zhou, H. Zhang, X. Tang, G. Sun, W. Huang, General metal-ion mediated method for functionalization of graphene fiber. *ACS Appl. Mater. Interfaces* **9**, 37022–37030 (2017).
54. P. Li, Z. Jin, L. Peng, F. Zhao, D. Xiao, Y. Jin, G. Yu, Stretchable all-gel-state fiber-shaped supercapacitors enabled by macromolecularly interconnected 3D graphene/nanostructured conductive polymer hydrogels. *Adv. Mater.* **30**, 1800124 (2018).
55. Q. Li, Q. Zhang, J. Sun, C. Liu, J. Guo, B. He, Z. Zhou, P. Man, C. Li, L. Xie, Y. Yao, All hierarchical core–shell heterostructures as novel binder-free electrode materials for ultrahigh-energy-density wearable asymmetric supercapacitors. *Adv. Sci.* **6**, 1801379 (2019).
56. Q. Liu, A. Zhao, X. He, Q. Li, J. Sun, Z. Lei, Z.-H. Liu, Full-temperature all-solid-state $Ti_3C_2T_x$/Aramid fiber supercapacitor with optimal balance of capacitive performance and flexibility. *Adv. Funct. Mater.* **31**, 2010944 (2021).
57. L. Lim, Y. Liu, W. Liu, R. Tjandra, L. Rasenthiram, Z. Chen, A. Yu, All-in-one graphene based composite fiber: Toward wearable supercapacitor. *ACS Appl. Mater. Interfaces* **9**, 39576–39583 (2017).
58. W. Nie, W. Weng, L. Liu, S. Zhang, X. Yang, J. Hu, Y. Zhang, Q. Li, X. Ding, Robust rope supercapacitor constructed by programmed graphene composite fibers with high and stable performance. *Carbon* **146**, 329–336 (2019).
59. Y. Jung, T. Kim, C. R. Park, Effect of polymer infiltration on structure and properties of carbon nanotube yarns. *Carbon* **88**, 60–69 (2015).
60. J. Shin, K. Lee, Y. Jung, B. Park, S. J. Yang, T. Kim, S. B. Lee, Mechanical properties and epoxy resin infiltration behavior of carbon-nanotube-fiber-based single-fiber composites. *Materials* **14**, 106 (2021).

Acknowledgments

Funding: This work was supported by the National Research Foundation of Korea (NRF) grant funded by the Korean government (MSIP) (nos. NRF-2021R1A4A2001403 and 2019R1A2C4069989). This research was supported by the Fundamental Research Program (PNK7340) of the Korea Institute of Materials Science (KIMS) and a grant from the Korea Institute of Science and Technology Open Research Program. This work was also supported by a Korea Evaluation Institute of Industrial Technology (KEIT) grant (20010853). This work was supported by the Technology Innovation Program (20006820) funded by the Ministry of Trade, Industry and Energy (MOTIE, Korea). **Author contributions:** T.K. and S.J.Y. conceived and supervised the research. Y.W.N., J.Y.C., and J.H.K. performed and analyzed the experimental data. Y.J., K.L., J.S.P., J.Y.P., K.S.S., and S.B.L. contributed to data analysis and manuscript editing. Y.W.N., J.Y.C., J.H.K., T.K., and S.J.Y. wrote the manuscript. All authors contributed to the discussion and paper preparation. **Competing interests:** The authors declare that they have no competing interests. **Data and materials availability:** All data needed to evaluate the conclusions in the paper are present in the paper and/or the Supplementary Materials.

Submitted 11 August 2021
Accepted 11 November 2021
Published 5 January 2022
10.1126/sciadv.abl8631